The Effects of Hydrolytic Weakening in Quartz-Rich Rocks from the Raft River Detachment Shear Zone

by

Trey Alexander Adams

A Thesis Submitted to the Graduate Faculty of Auburn University in partial fulfillment of the requirements for the Degree of Master of Science in Geology

Auburn, Alabama

May 2, 2026

Dr. Raphaël Gottardi (Chair), Associate Professor, Department of Geosciences

Dr. Laura Bilenker, Associate Professor, Department of Geosciences

Dr. Haibo Zou, Professor, Department of Geosciences

ABSTRACT

Hydrolytic weakening – the reduction of mineral strength in the presence of water – has long been invoked as a key mechanism controlling quartz rheology, yet its role in naturally deformed rocks remains debated. This study investigates the relationship between water content, fluid distribution, and deformation mechanisms in quartz-rich rocks from the Miocene Raft River detachment shear zone (Utah, USA). We analyze a suite of quartzite mylonites and quartz veins spanning a range of strain intensities and degrees of fluid-rock interaction. A comprehensive analytical approach combining optical petrography, scanning electron microscopy cathodoluminescence (SEM-CL), electron backscatter diffraction (EBSD), and Fourier transform infrared spectroscopy (FTIR) is used to characterize microstructures, crystallographic fabrics, and spatial variations in water content.

Microstructural observations indicate that quartz deformation is dominated by dislocation creep accommodated by subgrain rotation recrystallization across all sample types. FTIR data reveal systematic variations in water content, with the lowest concentrations in grain interiors and significantly higher concentrations along grain boundaries and within recrystallized domains. However, the most highly strained rocks (mylonites) exhibit overall lower water contents compared to less deformed vein samples. Cathodoluminescence imaging further demonstrates a strong correlation between luminescence intensity and deformation microstructures, with recrystallized grains consistently exhibiting lower CL intensity than relic grains.

These results suggest that hydrolytic weakening in natural systems is not simply controlled by bulk water content, but rather by the distribution of water within the rock, particularly its concentration along grain boundaries. These findings also demonstrate that progressive deformation, accommodated by dislocation creep and dissolution-precipitation, leads to redistribution and homogenization of the water content across the detachment shear zone. This work highlights the importance of microstructural controls on fluid localization and provides new constraints on the role of fluids in weakening mid-crustal shear zones.

ARTIFICAL INTELLIGENCE (AI) USE DISCLOSURE

In the preparation of this thesis, no Artificial Intelligence (AI) tools were used.

DIGITAL ACCESSIBILITY USE DISCLOSURE STATEMENT

In the preparation of this thesis dissertation, the following digital accessibility tools were used to ensure this document complies with federal requirements: Microsoft Word, Adobe Creative Cloud. The author acknowledges full responsibility for the intellectual content of this work and has made a good faith effort to comply with digital accessibility requirements in publishing, wherein the nature of the content does not significantly change in order to do so. Furthermore, all content has been reviewed and revised to meet these requirements prior to final publication.

TABLE OF CONTENT

LIST OF TABLES

LIST OF FIGURES

1. INTRODUCTION

Quartz is a crucial component of the Earth's crust. Its mechanical properties significantly influence geological processes such as rock deformation, fault mechanics, and seismic activity (e.g., Hirth et al., 2001; Bürgmann and Dresen, 2008). Among the various mechanisms affecting quartz's strength and ductility, hydrolytic weakening stands out as a key process (Griggs & Blacic, 1965; Griggs, 1967; Ave Lallemant and Carter, 1971; Tullis & Yund, 1980). Hydrolytic weakening refers to the reduction in the strength of quartz due to the presence of water (from ~100 to > 10,000 H/10^6 Si, Kilian et al., and references therein), either as fluid inclusions or structurally bound hydroxyl groups (e.g., Kronenberg et al., 2017) and has been observed in experiments on natural and synthetic quartz deformed at high temperature (Ghosh et al., 2024 and references therein). Yet, the mechanism remains heavily debated in naturally deformed rocks (e.g., Kilian et al., 2016; Kronenberg et al., 2020). Although "wet" flow laws match estimated flow stress and strain rates of naturally deformed rocks, there is no direct correlation between water content and strain magnitude consistent with observations from deformation experiments (e.g., Kronenberg et al., 2020).

Studies of naturally deformed rocks are rare and have shown mixed relationships between strain magnitude and water content, in some cases exhibiting a positive correlation (Kronenberg and Wolf, 1990; Nakashima et al., 1995; Gleason and DeSisto, 2008), a negative correlation (e.g., Kilian et al., 2016; Kronenberg et al., 2020), or no correlation at all (Ceccato et al., 2022; Pongrac et al., 2024). Therefore, additional work on naturally deformed rocks is needed to determine the role of hydrolytic weakening on quartz deformation.

The primary objective of this research project is to image water distribution and measure water content as a function of strain in the quartz-rich rocks from the well-studied Miocene Raft River detachment shear zone (RRDSZ). The presence of fluid and fluid-rock interactions during the formation and exhumation of the RRDSZ is ubiquitous (Gottardi et al., 2011, 2024; Methner et al., 2015) and has been proposed as a strain weakening mechanism (Gottardi et al., 2015) but never confirmed. By examining how the water enters the rocks, where it is located, and how it affects the mechanical properties of the rock, we aim to expand our understanding of fluid-rock-deformation interactions in extensional systems. This research will be conducted using a novel analytical approach that has not been applied in the RRDSZ, specifically combining scanning electron microscopy cathodoluminescence (SEM-CL) and Fourier Transform Infrared (FTIR)

spectroscopy to petrographic microstructural analysis and electron backscatter diffraction (EBSD). The results of this research are intended to improve our understanding of the impact of the presence water during deformation, which has direct implications for our understanding of strain localization processes and the rheology of the crust.

2. HYDROLYTIC WEAKENING IN QUARTZ

2.1.Hydrolytic weakening in experiments

Hydrolytic weakening has long been recognized as a key weakening mechanism in laboratory deformation experiments (Griggs & Blacic, 1965; Griggs, 1967; Ave Lallemant and Carter, 1971; Tullis & Yund, 1980). However, recent studies challenge that concept. For example, detailed work by Ceccato et al. (2022) investigated the strength of both wet (20–100 wt ppm H_2O) and dry (<20 wt ppm H_2O) quartz under low temperature conditions (200–300°C) through nanoindentation, a technique designed to test the hardness and elasticity of a material. Results indicate that different water contents do not affect the strength of quartz under these experimental conditions. Rather, the authors suggest that the high density of defects within crystals may control the strength of quartz rather than water content, but they do not reject the effect of higher fluid contents than those tested in the study (>100 wt ppm H_2O). Recently, Stünitz et al. (2024) conducted an experimental study to investigate how water in quartzite affects its mechanical properties during high temperature deformation (900°C) at varying pressure amounts (600–2000 MPa). Results showed systematically higher water content (molar proportions of H atoms per 10^6 Si atoms or H/10^6 Si) content at grain boundaries than in grain interiors. The authors explained this observation by water transfer from fluid inclusions in the interiors to the grain boundaries by microcracking and advective processes, including potential transport via dislocations (Stünitz et al., 2024). However, this behavior did not correlate with changes in confining pressure, suggesting that this mechanism does not seem to be pressure or stress dependent. The authors infer that for naturally deformed quartzites, as long as water is retained in the grain boundary regions, the internal water content of most natural samples will be sufficient to facilitate quartz deformation (Stünitz et al., 2024).

2.2.Hydrolytic weakening in naturally deformed rocks

The concept that high water content promotes intracrystalline deformation through hydrolytic weakening is also challenged by recent analyses of naturally deformed rocks. For example, several studies demonstrate an inverse correlation between deformation intensity and water content (Kilian et al., 2016; Palazzin et al., 2018; Kronenberg et al., 2020; Rahl et al., 2024). All these publications suggest that the presence of water at grain boundaries, rather than the amount of water, may govern hydrolytic weakening, an observation similar to findings from the experimental work discussed above.

3. REGIONAL GEOLOGY: THE RAFT RIVER METAMORPHIC CORE COMPLEX AND DETACHMENT SHEAR ZONE

The Raft River Mountains of Northwest Utah make up the eastern portion of the much larger Albion-Raft River-Grouse Creek metamorphic core complex (Figure 1). The Raft River Mountains are comprised of Archaean-Permian aged metamorphic rocks that were deformed under amphibolite-greenschist facies conditions (Compton, 1980; Wells, 1997, Wells et al., 2000; Gottardi et al., 2011, 2015, Gottardi and Teyssier, 2013). The mountain range contains two separate shear zones, the Eocene-Oligocene Middle Mountain shear zone to the west and the younger Oligocene-Miocene RRDSZ to the east – this study focuses on the latter. The ~100m thick Miocene RRDSZ is localized in the mylonitized Proterozoic Elba Quartzite that exhibits a finite strain gradient along the transport direction (e.g., Wells, 1997; Sullivan, 2008). A detachment fault separates the footwall mylonite from the Neoproterozoic-Paleozoic hanging wall, that is only preserved in isolated klippen.

The Elba Quartzite is on average composed of ~90% quartz and ~10% muscovite. The microstructures characteristic of the RRDSZ have been extensively described by Compton (1980), Wells (1997), Wells et al (2000), Gottardi et al. (2011, 2015), Gottardi and Teyssier (2013) and Gottardi and Hugues (2022) and summarized below. The quartzite mylonite exhibits characteristic dislocation creep microstructures associated with subgrain rotation recrystallization (regime 2 of Hirth and Tullis, 1992). Small (25 – 75 μm) recrystallized grains typically surround large (> 500 μm) relic grains with moderate aspect ratios (1:2 to 1:5) oriented parallel and defining the mylonitic foliation. Relic grains exhibit high stress/high strain rate microstructures

such as undulose extinction and deformation lamellae, indicating that recovery processes were not efficient enough to dissipate the internal energy stored in the quartz grains and keep up with strain rate and offset strain hardening. Up to 50% of the studied thin sections consist of recrystallized grains (Gottardi and Teyssier, 2013). Microstructural results and quartz-muscovite oxygen stable isotope geothermometry suggest deformation temperatures ranging from 350 to 375°C (Gottardi et al., 2011).

The RRDSZ is also cut by several generations of quartz veins showing varying degrees of deformation. Gottardi et al. (2024) identified three dominant sets of veins: high angle veins (dip angle ~70°), low angle veins (dip angle of ~20°), and transposed veins (~10°, subparallel to foliation). Microstructurally, the high angle veins are characterized by large lozenge-shaped quartz grains, commonly forming ribbons characterized by sweeping undulose extinction and abundant deformation lamellae. Minor dynamic recrystallization by subgrain rotation can be found at boundaries of the larger grains. Low angle veins exhibit a foliated texture expressed by large ribbon grains oriented sub-parallel to the mylonitic foliation. Dynamic recrystallization by subgrain rotation is evident and affects up to 40% of the vein area of the thin sections. Large ribbons are nearly entirely recrystallized by subgrain rotation in the transposed veins, leaving only a few relic grains.

Microstructural analysis of quartzite mylonite and quartz veins by Gottardi and Hughes (2022) and Gottardi et al. (2024) reveal the presence of several fluid-related microstructures, including healed microcracks, transgranular fluid inclusion planes, and grain boundary fluid inclusion clusters, that we summarize in the following. Healed microfractures are abundant in the quartzite mylonite and typically cut the mylonitic foliation at high angle (>70°). They range from ~20 to 100 μm in width and are filled with recrystallized quartz. Fluid inclusions are abundant in these fractures and on offshoot fluid inclusion planes, as well as in horsetail structures at the tip of the fractures. Transgranular fluid inclusion planes crossing multiple grains are abundant through. They typically occur in parallel and conjugate sets oriented at high angle to the mylonitic foliation. These planes contain a large amount of fluid inclusions (100 – 1000s). Lastly, grain boundary fluid inclusions are found around recrystallized quartz grains and typically outline subgrain boundaries in large relic grains. These are quite common in the quartzite mylonite.

Fluid-rock-deformation interactions have been extensively studied in the RRDSZ through oxygen and hydrogen stable isotope geochemistry of quartz, muscovite, and fluid inclusions

(Gottardi et al., 2011, 2015, 2024; Methner et al., 2015). These studies have demonstrated the abundant and prolonged presence of fluids during evolution of the Raft River detachment shear zone. Hydrogen isotope analyses of fluid inclusions in quartz and synkinematic muscovite indicate that mylonitization occurred in the presence of a fluid characterized by low $^{2}H/^{1}H$ and $^{18}O/^{16}O$, typical of meteoric origin ($-100‰ < \delta^{2}H_{fluid} < -70‰$) (Gottardi et al., 2011; 2015; 2024). Together, structural, microstructural, and geochemical observations suggest that meteoric fluid permeated the RRDSZ near the brittle-ductile transition (~10-12 km depth), and that the shear zone experienced episodic influxes of fluids through semi-brittle structures. This fluid was then expelled into the surrounding mylonite following progressive shearing, causing further ^{18}O-depletion of the quartzite and fluid-related embrittlement of the shear zone (Gottardi and Hughes, 2022; Gottardi et al., 2024). Therefore, the Raft River detachment shear zone is an excellent natural laboratory to investigate how fluids interact with recrystallizing quartz in the ductile regime, and its potential hydrolytic weakening effect on quartz.

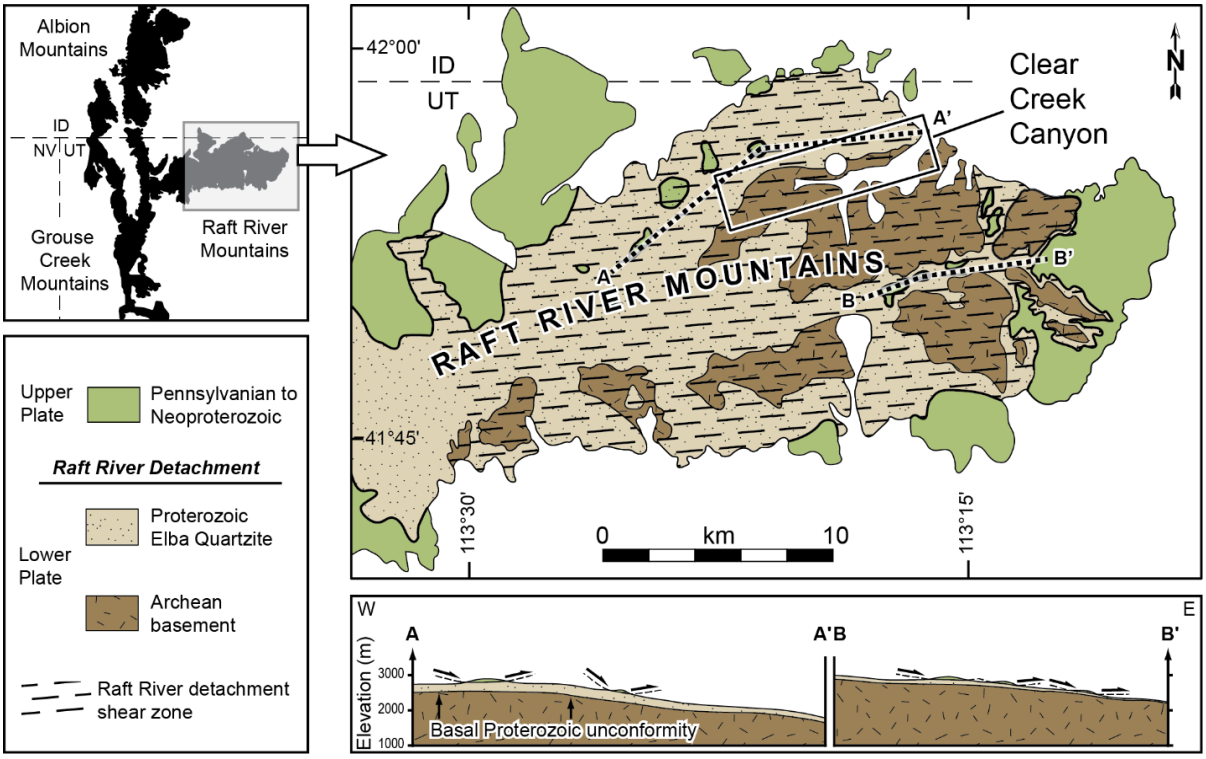

Figure 1: Simplified geologic map of the Raft River Mountains and associated Miocene Raft River detachment shear zone. The study area is located in the Clear Creek Canyon (from Gottardi et al. 2024).

4. METHODOLOGY

4.1.Sample Selection and Preparation

The samples used in this study were selected from Gottardi et al. (2024) based on their texture (vein vs. mylonite) and their stable isotope signature (Figure 2, Table 1). Since our goal is to investigate the role of water in quartz recrystallization (hydrolytic weakening), we decided to select a suite of samples that show various degrees of fluid-rock interaction (evaluated through quartz-muscovite stable isotope analyses) and various amounts strain (estimated based on the amount of recrystallization, e.g., Cross and Skemer, 2019). Here is the rationale behind our sample selection.

- **High Strain / Low fluid-rock interaction:** we selected four mylonite samples with some of the highest quartz and muscovite $\delta^{18}O$ values, representing mylonite samples that interacted the **least** with a meteoric fluid (RR09-125, -128, -132, -135).
- **High Strain / High fluid-rock interaction:** four mylonite samples with some of the lowest quartz and muscovite $\delta^{18}O$ values, which represent mylonite samples that interacted the **most** with a meteoric fluid (RR09-10, -11, -13, -15).
- **Moderate Strain / Low fluid-rock interaction:** we selected two samples of transposed quartz veins (moderately recrystallized) with the highest quartz $\delta^{18}O$ values (RR21-37, -45).
- **Moderate Strain / High fluid-rock interaction:** we selected two samples of transposed quartz veins (moderately recrystallized) with the lowest quartz $\delta^{18}O$ values (RR21-01, -69)
- **Low Strain / High fluid-rock interaction:** we choose one sample of the high angle veins (incipient recrystallization) with the lowest quartz $\delta^{18}O$ value (RR21-60).

Billets of all these samples were cut and sent to Spectrum Petrographic for thin section preparation. FTIR analyses requires thicker than usual thin sections, typically 80 μm, and doubly polished wafers. In the following we refer to them as “thick sections”.

Table 1: Summary of geochemical data from Gottardi et al. (2024). Oxygen isotope results of quartz ($\delta^{18}O_{qtz}$) and muscovite ($\delta^{18}O_{ms}$), oxygen isotope fractionation between quartz and muscovite ($\Delta^{18}O_{qtz\text{-}ms}$), temperature of equilibrium calculated based on Chacko et al. (1996) quartz-muscovite calibration, and hydrogen isotope results of muscovite ($\delta^{2}H_{ms}$). $\delta^{18}O$ and $\delta^{2}H$ values are reported relative to SMOW; error is ± 0.08‰ (1σ) and ± 2‰ (1σ) for oxygen and hydrogen, respectively, based on the reproducibility of standards from the analytical runs.

Sample	$\delta^{18}O_{qtz}$ (‰)	$\delta^{18}O_{ms}$ (‰)	$\Delta^{18}O_{qtz\text{-}ms}$ (‰)	T (ºC)	$\delta^{2}H_{ms}$ (‰)
		Transposed Quartz Veins			
RR21-01	**10.1**	**7.5**	**2.6**	**460**	**-125**
RR21-11	11.5	8.3	3.2	390	-106
RR21-18	11.5	7.8	3.7	350	-112
RR21-37	**12.1**	**9.5**	**2.6**	**460**	**-108**
RR21-45	**12.1**	**8.7**	**3.4**	**370**	**-88**
RR21-69	**9.1**				
		High Angle Quartz Veins			
RR21-40	10.1				
RR21-47	10.6				
RR21-53	11.0				
RR21-60	**10.7**				
		Quartzite Mylonite from the Notch			
RR09-10	**10.8**	**10.1**	**0.7**		**-100**
RR09-11	**11.0**	**10.1**	**0.9**		**-101**
RR09-12*	11.5	8.0	3.5	360	-83
RR09-13	**11.6**	**11.2**	**0.4**		**-77**
RR09-14	11.4	10.4	1.0		-86
RR09-15	**11.8**	**10.4**	**1.4**		**-77**
RR09-18*	12.4	8.3	4.1	310	-101
RR09-19*	11.2	7.8	3.4	370	-110
		Quartzite Mylonite			
RR09-136	11.7	10.5	1.2		-105
RR09-135	**12.6**	**10.6**	**2.0**		**-112**
RR09-134	12.7	11.5	1.2		-110
RR09-133	12.7	9.5	3.3		-123
RR09-132	**13.0**	**12.1**	**0.9**		**-104**
RR09-131	12.8	11.5	1.3		-110
RR09-130	12.8	10.8	2.0		-112
RR09-129	12.8	10.2	2.6		-101
RR09-128	**12.8**	**10.5**	**2.3**		**-103**
RR09-127	12.8	10.6	2.2		-107
RR09-126	12.6	9.6	3.1		-111
RR09-125	**12.7**	**10.7**	**2.0**		
RR09-124	13.1	11.6	1.4		-102
RR09-123	13.4	11.1	2.3		-106
RR09-122	13.6	11.5	2.1		

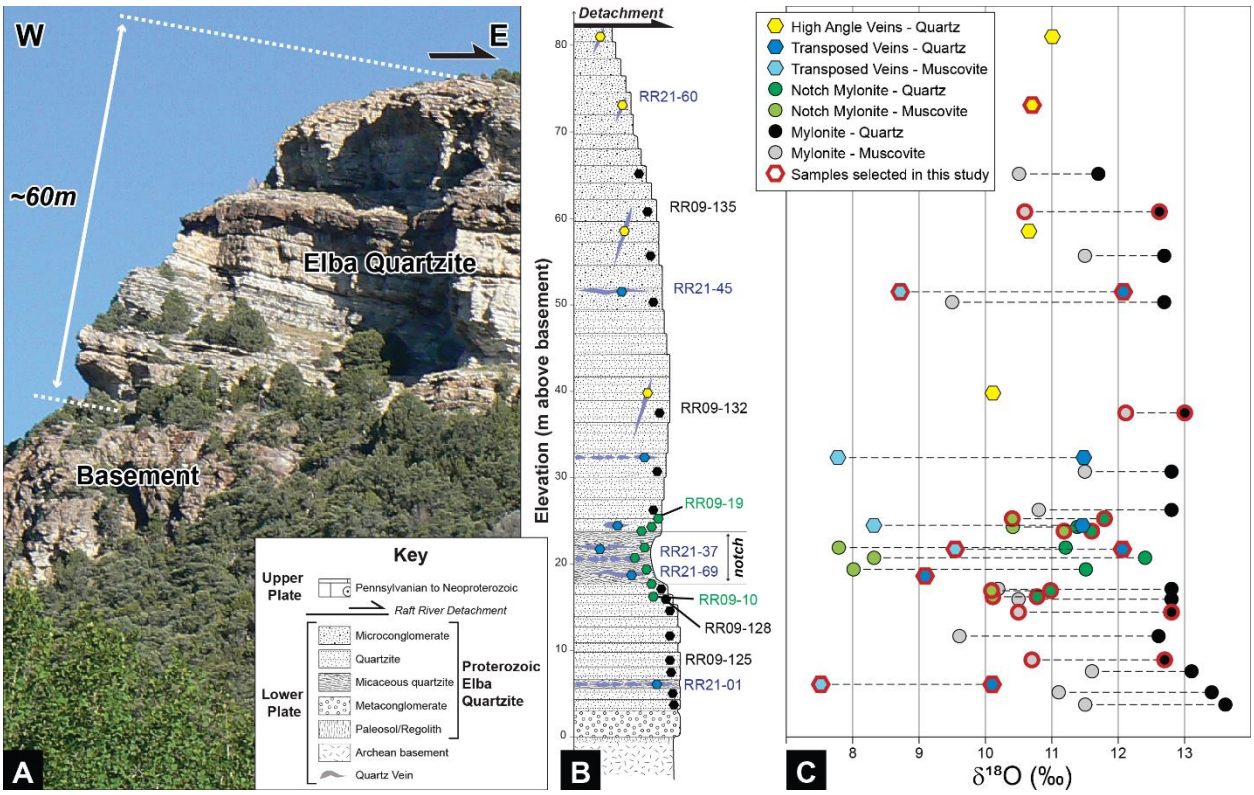

Figure 2: (**A**) Picture of the RRDSZ at Clear Creek Canyon. (**B**) Vertical profile through the RRDSZ showing sample locations. (**C**) Summary of previously published stable isotope data on the RRDSZ from Gottardi et al. (2024). The samples selected for this study are outlined in red in (C).

4.2.Optical Petrography

The final analytical step in our analytical sequence – FTIR spectroscopy – has to be conducted on the doubly polished wafers of rocks removed from the support glass slide, effectively destroying the thick sections. Therefore, great care was taken in documenting the thin sections at various scales before proceeding to FTIR analyses. The first step was to use a Nikon CoolScan 5000 to produce full thin section scan. Subsequently, a Nikon LV100 Polarizing Microscope and Nikon DS-10 camera were used to produce high resolution photomosaic of each sample. Thorough documentation of the quartz microstructures was then conducted at varying magnifications.

4.3.Scanning Electron Microscopy Cathodoluminescence (SEM-CL)

Cathodoluminescence (CL) refers to the emission of photons from a material when exposed to a high energy electron beam. The characteristics of the light spectrum emitted by CL can reveal internal textures, growth history, and chemical variations not visible with standard microscopy (e.g., Rusk et al., 2006; Parish and Russell, 2007). In particular, the wavelength and intensity of the emitted light are influenced by defects and trace elements within the crystal structure of minerals, which can be used to infer information regarding crystal growth, formation, deformation, and fluid-rock interaction (e.g., Frelinger et al., 2015).

Polished thin sections were first coated in 5 nm carbon using a JOEL EC-32010CC carbon coater. Cathodoluminescence scans of each sample were then collected using a Zeiss EVO 15 SEM operated in high vacuum mode and equipped with a Zeiss Cathodoluminescence detector. Typical operating conditions for imaging were a 20 keV accelerating voltage and 1-5 nA of beam current and a working distance of 8.5 mm.

4.4.Scanning Electron Microscopy Electron Backscatter Diffraction (SEM-EBSD)

SEM-EBSD is a powerful technique used to investigate the microstructural and crystallographic properties of rocks and minerals. EBSD provides high-resolution images of mineral textures, such as crystallographic preferred orientation, grain and subgrain boundaries, and grain misorientation. EBSD data are used to study deformation mechanisms, recrystallization processes, and the evolution of rock fabrics during deformation. EBSD is time-consuming to acquire, so we acquire EBSD data only from small areas within each sample. These areas were selected based on the microstructures identified through petrographic analysis and CL scans.

EBSD data were collected on the same Zeiss EVO 15 SEM using 20 kV accelerating voltage and 20 to 60 nA beam current. EBSD patterns were collected on an Oxford AZtecHKL EBSD C-Nano and processed and indexed using Oxford Instruments AZtec software. Each sample was mapped at step sizes ranging from 2 to 6 μm.

4.5.Fourier Transform Infrared Spectroscopy (FTIR)

FTIR is used to analyze the molecular structure and chemical composition of a material. It works by measuring how a sample absorbs infrared light at specific wavelengths. Infrared light is emitted from the machine onto a sample before being absorbed by the molecules within the sample (Berthomieu and Hienerwadel, 2009). The molecules vibrate differently depending on how much light is absorbed, which is influenced by what the composition of the individual molecule is. The detector then identifies the frequencies that the molecules vibrate at, before automatically compiling them into a spectrum that displays the intensity of absorbed light as a function of frequency. This absorption spectrum will include various peaks at specific wavelengths that correspond to specific compounds. By analyzing this plot with a knowledge of how a molecule absorbs infrared light, one can then determine the chemical composition of a sample. In our project, we focus mainly on two primary wavelength peaks: ~3400 cm^{-1} and ~1650 cm^{-1}. The broad band at ~3400 cm^{-1} is characteristic of OH from molecular water, while the ~1650 cm^{-1} is associated with water (H_2O) trapped in fluid inclusions (Kronenberg et al., 2017). The ~3400 cm^{-1} peak is associated with molecular water in in quartz, and variations in the ~3400 cm^{-1} band correlate with variations in water content, where the area under the peak is proportional with the amount of water in quartz (e.g., Kronenberg et al., 2017).

The FTIR analyses were conducted at the Advanced Light Source (ALS), housed at the Lawrence Berkeley National Laboratory in Berkely, California. Due to technology issues, analyses could not be conducted using the synchrotron FTIR. Instead, we used a FTIR microscope that fitted our analyses. This analytical equipment is composed of an Agilent Technologies Cary 670 FTIR Spectrometer attached to a Cary 620 IR Microscope. Data collected on the spectrometer was initially viewed via the Resolutions Pro Software package that is pre-installed with the equipment. Data processing was done using Quasar (Demsar et al., 2013). Quasar is an open-source software that allows for the processing, visualization, and interpretation of raw data such as the FTIR data collected at the ALS.

Water content estimations were based on the integrated area of the broad absorbance peak at ~3400 cm^{-1}, measured above a linear baseline between 3550 and 3450 cm^{-1}. Integrated absorbance of OH bands at 3400 cm^{-1} is used to determine OH content in our samples using the Beer-Lambert equation (Stuart et al., 1996):

$$C_w = \frac{M_w\, A}{\rho\, t\, \varepsilon}$$

where C_w is the concentration of OH (in molar ppm, OH/10^6Si), M_w is the molecular weight of OH (17.007 g/mol), A is the absorbance height of the peak of interest (3400 cm^{-1}), ρ is the density of quartz (2.65 $g.cm^{-3}$), t is the thickness of the area analyzed (cm), and ε is the molar absorptivity of quartz (78 $L.mol^{-1}.cm^{-1}$) (Hetherington, 1962; Paterson, 1982). We use an average thickness of 80 µm. The greatest sources of uncertainty in this calculation is the sample thickness, which was only estimated, and the absorption coefficient of OH in quartz. Note that there are several other calibrations to convert absorbance to concentration that may lead to different absolute results (see review by Fukuda and Shimizu, 2019 and Stünitz et al., 2024). Another point of caution, in the conversion, is the use of either absorbance measured in a single section of the mineral, or total absorbance, as noted by Stünitz et al. (2024), which may lead to significant differences in absolute numbers. Given all these conditions and limitations of H-measurements, the determination of H_2O is semi-quantitative, i.e., absolute numbers are given for relative comparison only.

5. RESULTS

5.1. Microstructural analysis

First, we conducted a microstructural analysis of our samples to identify (1) the dominant recrystallization mechanisms for quartz, (2) potential fluid pathways, and (3) distribution of fluid inclusions. Our results add to previous characterizations by Gottardi and Hughes (2022) and Gottardi et al. (2024). As a reminder, we use the degree of recrystallization of our samples as a proxy for strain. As such, we interpret our high angle veins, low angle veins, and mylonite to reflect low, moderate, and high strain, respectively.

5.1.1. Quartz Microstructures

The high-angle quartz veins are dominantly composed of blocky quartz grains (80-90%), and minor recrystallized grains (10-20%). The blocky grains tend to be large (1-10 mm) and lozenge-shaped and are characterized by wide extinction bands and some quartz ribbons (e.g., Derez et al., 2015) producing sweeping undulose extinction across grains (Figure 3). Low angle deformation bands commonly cut across large grains and are associated with numerous subgrains suggesting incipient recrystallization (Figure 3). The majority of these large grains exhibit deformation lamellae, the quartz ribbons especially, and transgranular fluid inclusion trails. In these high angle veins, the recrystallized grains occur along deformation bands, and range in size from sub-micron to ~250 μm. The recrystallized grains are relatively equant with serrated boundaries and are directly associated with subgrains, suggesting that the dominant recrystallization mechanism was subgrain rotation (Regime II of Hirth and Tullis, 1992). Shear bands are locally associated with very fine (sub-micron) to comminuted grains, which typically form by brittle cataclasis, suggesting that these high angle veins may have evolved close to the brittle-ductile transition.

In the low-angle quartz veins, the blocky texture characteristic of the high angle veins is no longer present. Instead, the texture is characterized by large quartz ribbons separated by wide deformation bands and swaths of recrystallized grains (Figure 4). The large ribbons (1-5 mm long, 1-2 mm thick) are characterized by the same sweeping undulose extinction and deformation lamellae than in the high angle veins. The ribbons and bands of recrystallized grains are typically oriented sub-parallel to the mylonitic foliation (Figure 4). The boundaries of quartz ribbons show patchy undulose extinction, and subgrains have again a direct relationship with subgrains, suggesting that quartz in these low-angle veins recrystallized by the same deformation mechanism: subgrain rotation. The recrystallized grains have approximately the same size as in the high angle veins (20–250 μm). Recrystallized grains form an oblique secondary foliation, oriented at 20-30° from the mylonitic foliation, consistent with a top-to-the-east sense of sear. Dynamic recrystallization affects up to 40% of the vein area of the thin sections.

The quartzite mylonites microstructures exhibits a bimodal grain population: coarse, elongate relic grains and recrystallized grains (Figure 5). Relic grains (250 – 1000 μm) are elliptical, with their long axis parallel to the mylonitic foliation, and aspect rations ranging from 1:2 to 1:10. They display undulose extinction and often exhibit deformation lamellae. The rims of relic grain

show numerous patchy subgrains, that matches recrystallized grains, suggesting that once again, quartz recrystallization was accommodated by subgrain rotation recrystallization. In the mylonite samples, muscovite grains are typically oriented parallel to and defining the mylonitic foliation. Up to 60% of the mylonitic samples consist of recrystallized grains.

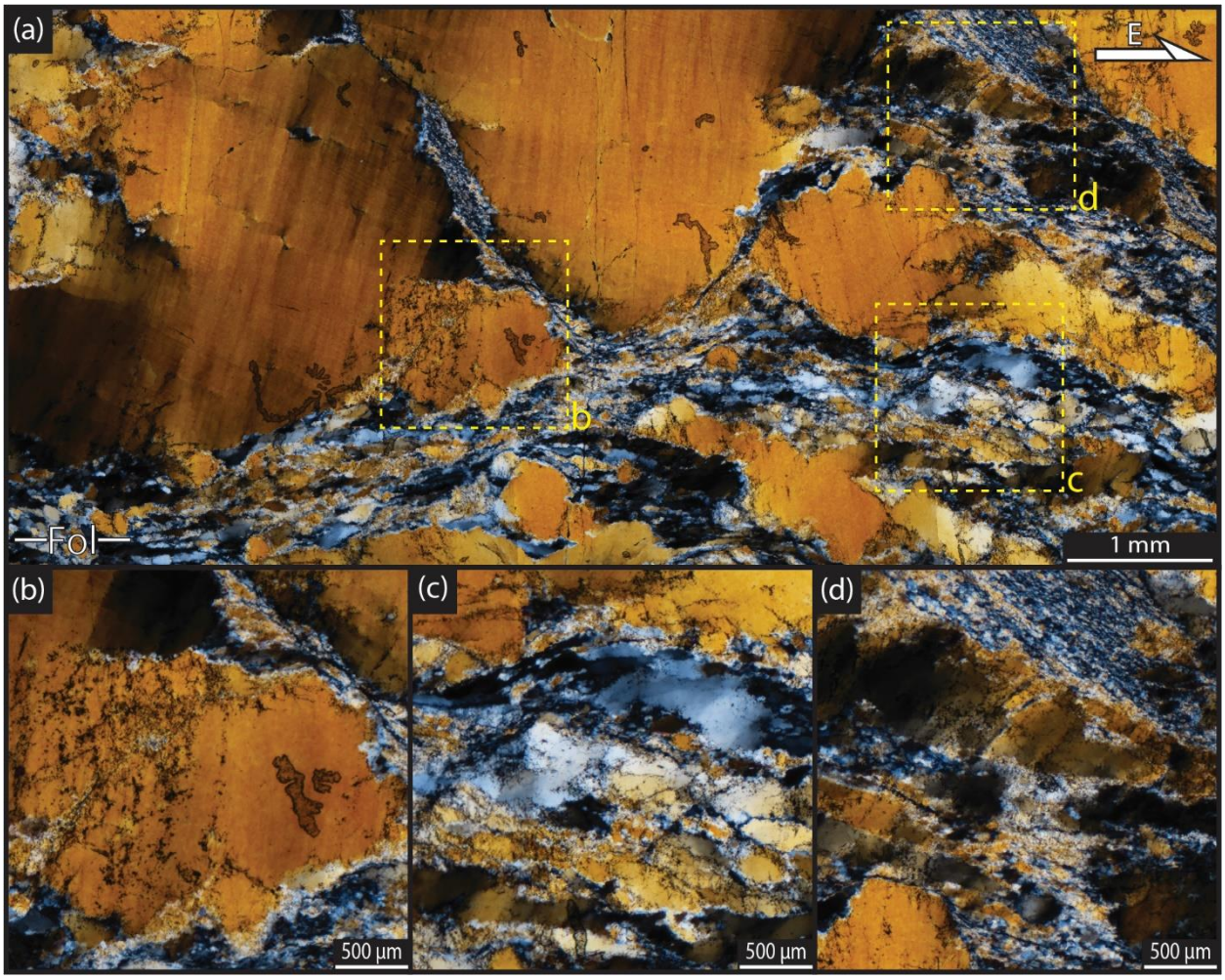

Figure 3: Photomicrographs of characteristic microstructures of high angle quartz veins (sample RR21-60). **(a)** Area showing large blocky lozenge-shaped grain as well as finely comminuted/recrystallized areas. Note sweeping undulose extinction of the large grains. **(b)** Detail of large fluid inclusion clusters. **(c)** Relic grain surrounded by subgrain and recrystallized grains, indicating incipient subgrain rotation recrystallization. **(d)** Finely recrystallized/comminuted grains, possibly formed by cataclasis. Photomicrographs are oriented perpendicular to the foliation and parallel to the lineation.

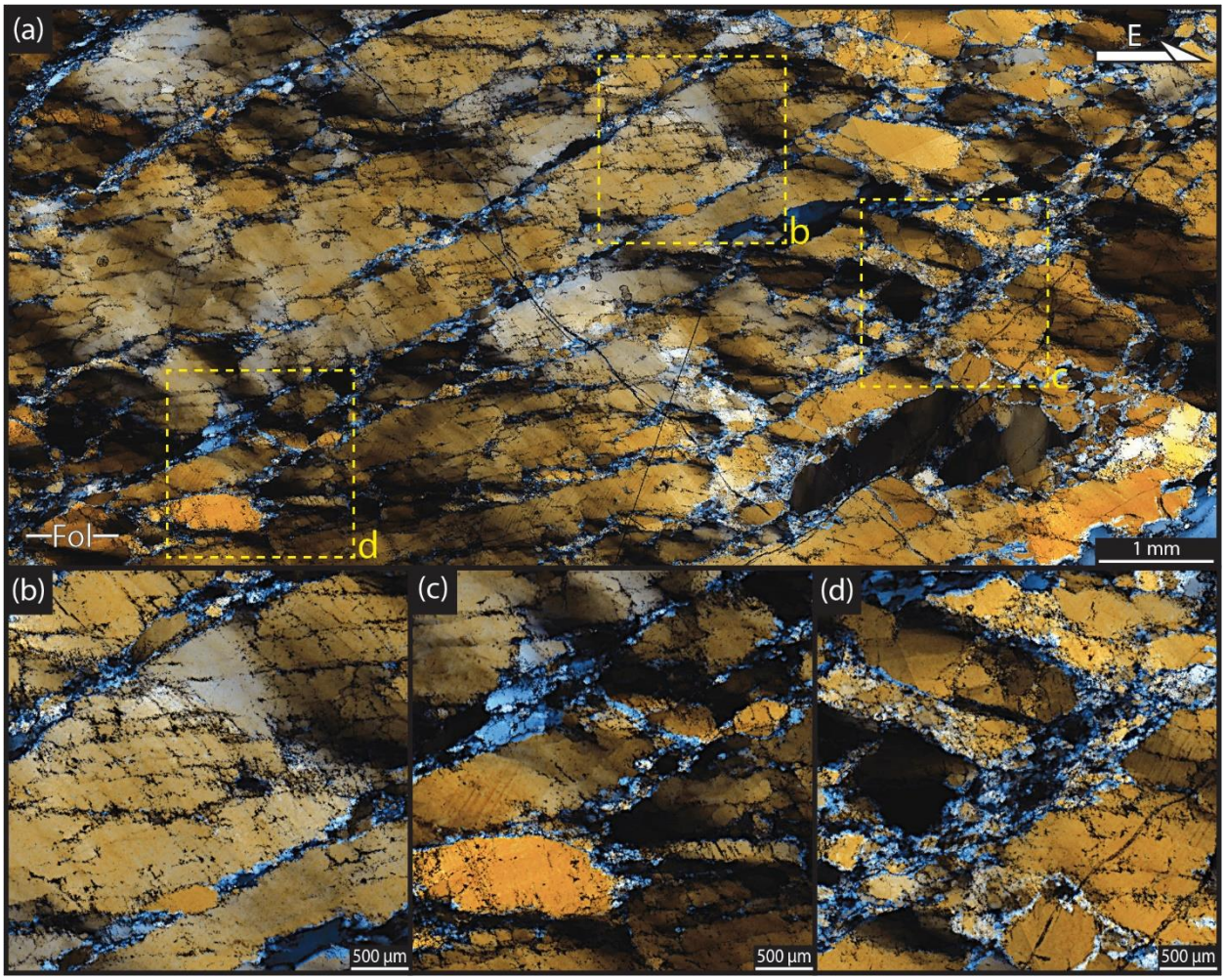

Figure 4: Photomicrographs of characteristic microstructures of low angle quartz veins (sample RR21-45). **(a)** Low angle quartz veins typically exhibit elongated quartz ribbons with sweeping undulose extinction, separated by wide extinction bands consisting of finely recrystallized grains. Note the abundance of intergranular fluid inclusion trails. **(b)** Details of intergranular fluid inclusion trails. **(c)** Recrystallized grains form by subgrain rotation recrystallization. Note deformation lamellae. **(d)** Fluid inclusions are also found in abundance in the recrystallized quartz grains. Photomicrographs are oriented perpendicular to the foliation and parallel to the lineation.

Figure 5: Photomicrographs of characteristic microstructures of quartzite mylonites (sample RR21-11). **(a)** Area showing large blocky lozenge-shaped grain as well as finely comminuted/recrystallized areas. Note sweeping undulose extinction of the large grains. **(b)** Detail of large fluid inclusion clusters. **(c)** Relic grain surrounded by subgrain and recrystallized grains, indicating incipient subgrain rotation recrystallization. **(d)** Finely recrystallized/comminuted grains, possibly formed by cataclasis. Photomicrographs are oriented perpendicular to the foliation and parallel to the lineation.

5.1.2. Fluid Inclusion Microstructures

Gottardi and Hughes (2022) previously investigated the fluid inclusions found in the Raft River detachment shear zones and describe three general fluid inclusion populations: (1) ones found in healed microfractures, (2) transgranular fluid inclusion planes, and (3) grain boundary fluid inclusions. Although the distribution of these populations varies across samples, our observations match that of Gottardi and Hughes (2022).

Healed Microfractures – Healed microfractures are common in both high angle and transposed veins, but rare in the quartzite mylonite. They typically form *en échelon* semi-rectilinear segments that cut a across the samples. They are typically oriented at high angle to the mylonitic foliation (> 50°), with a width of a few tens of microns. The microfractures are filled with quartz. Fluid inclusions are abundant in the quartz fill, but also in areas adjacent to the microfractures. Microfractures commonly end with horsetail structures associated with large number of fluid inclusions.

Transgranular Fluid Inclusion Planes – Fluid inclusion planes crossing multiple grains (transgranular) are common in all samples, but particularly abundant in the veins. They typically cut across quartz ribbons, and form systematic sets, oriented at ~30°-40°±10° and 140°-170° to the mylonitic foliation. These transgranular planes can be several hundreds of microns long and are typically decorated with many fluid inclusions (>100s).

Grain Boundary Fluid Inclusions – Clumps of fluid inclusions at grain and subgrain boundaries are the most abundant type of fluid inclusions in all samples. In the mylonitic samples, these types of fluid inclusions are typically found around recrystallized quartz grains and subgrain boundaries in relic grains.

5.2.Cathodoluminescence

The SEM-CL imaging in this study produced greyscale images showing various textures across all three sample types. The greyscale ranges from black to white, with darker colors indicating low luminescence and white indicating high luminescence (Figures 6-7). Although the range of luminescence in each sample varies, there are similarities between each sample type. The quartz veins tend to have a broader CL variability compared to the mylonites (Figure 6). Overall, the observed patterns show similarities to microstructures observed on the petrographic microscope.

First, across all samples, fractures are the most luminescent features (Figure 6). Since we are working with doubly polished thin sections, it is unknown whether this high luminescence is caused by leftover adhesive permeating the fracture, or by fluid inclusions or trace elements dispersed in the fracture infill. Petrographic imaging does not suggest that there is any residual adhesive (Figure 6), however, it is hard to exclude based on petrographic observations alone.

Second, muscovite appears very dark in CL compared to the surrounding quartz, making it easy to identify in the mylonite samples (Figure 7). However, there is a possibility that very fine-grained recrystallized muscovite could be present dispersed in fine grained recrystallized quartz, contributing to the darker luminescence in these areas as well (Figure 6A for example).

In the high-angle quartz veins, large lozenge-shaped blocky grains tend to have bright interiors, while bands of finely recrystallized grains tend to be darker (Figure 6A). Some of the larger grains of quartz also exhibit areas of higher luminescence within their interiors, though the localities of these high luminescence areas appear to vary across the grains. The bands of comminuted grains and recrystallized grains tend to be much darker. Other features, such as undulose extinction and deformation lamellae seem to also be reflected in the CL signal.

The transposed quartz vein samples show similar CL pattern that highlights the deformation textures. Relic grains tend to be bright, recrystallized grains are dark (Figure 6C). Deformation lamellae are nicely visible (Figure 6C).

The CL texture becomes more subdued in the quartzite mylonite, where the variability in CL intensity is not as extensive as in the veins (Figure 7). However, the CL pattern seems to closely match the microstructures: CL reveals recrystallized grains that tend to be darker than relic grains. The core of relic grains shows the highest CL and systematically exhibit a darker rim (Figure 7).

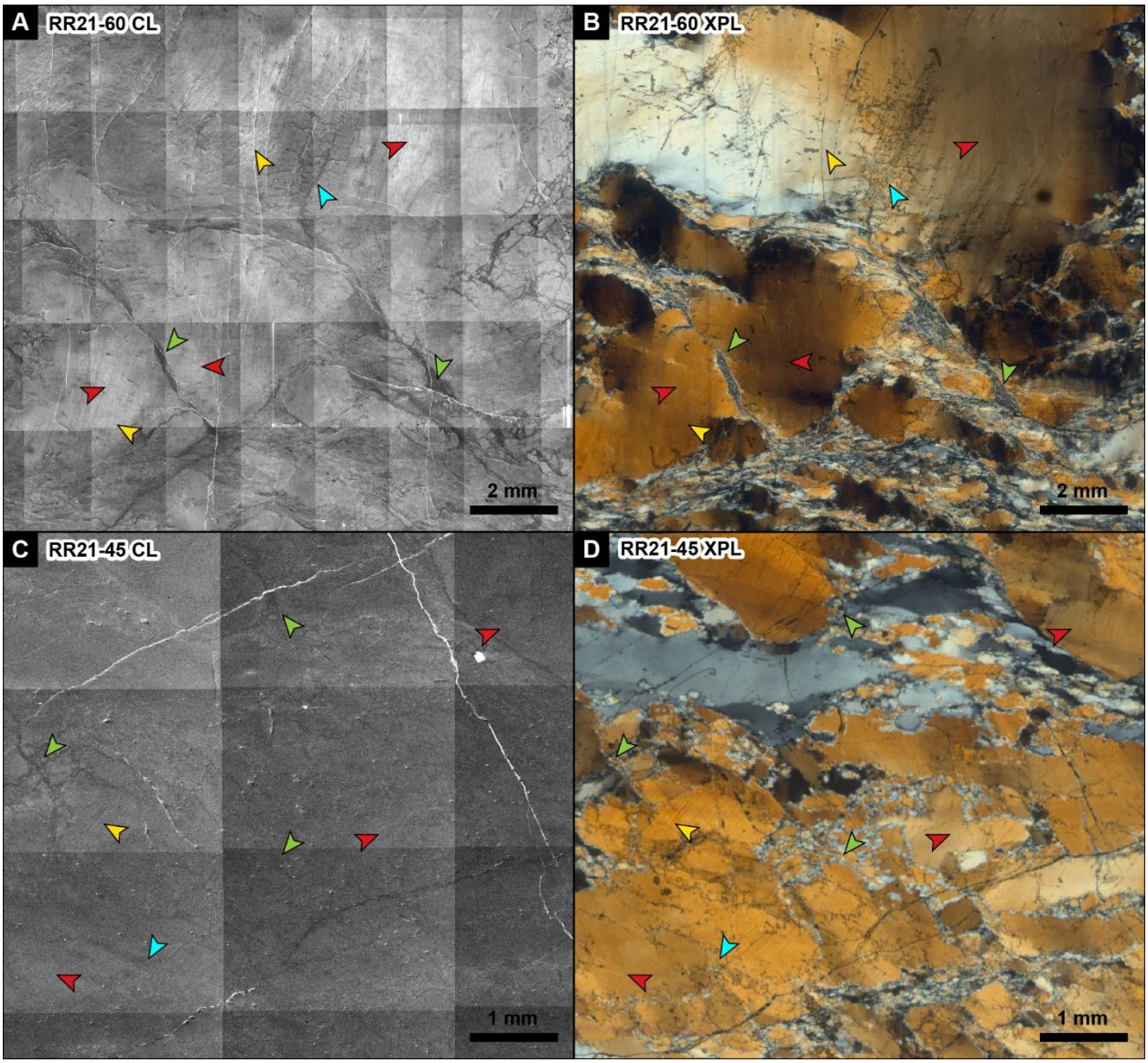

Figure 6: (A, C) Cathodoluminescence (CL) images and (B, D) corresponding cross-polarized photomicrographs (XPL) of representative high angle and low angle quartz veins, respectively (RR21-60 and RR21-45). Red arrows = grain cores, green arrows = recrystallized grains, yellow arrows = deformation lamellae; blue arrows = fluid inclusions.

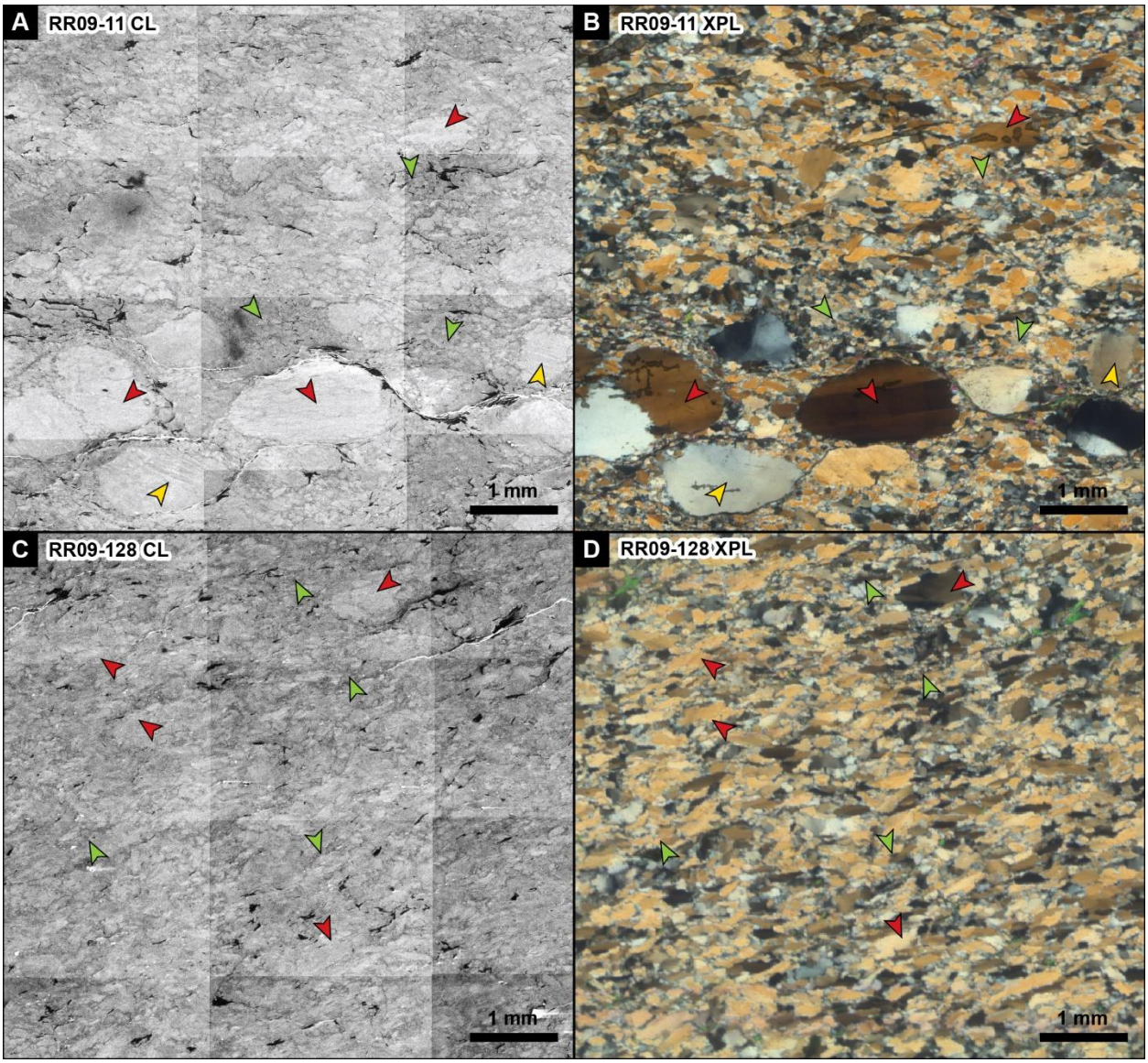

Figure 7: (A, C) Cathodoluminescence (CL) images and (B, D) corresponding cross-polarized photomicrographs (XPL) of representative quartzite mylonites (RR09-11 and RR09-128). Red arrows = grain cores, green arrows = recrystallized grains, yellow arrows = deformation lamellae

5.3.EBSD results

EBSD data was acquired to characterize grain and subgrain boundaries, in order to create grain boundary maps to help us interpret CL and FTIR results. Because acquiring EBSD data is tedious and time consuming, we only analyzed smaller areas within selected representative samples. We then were able to overlap the analyzed area with petrographic images, CL and FTIR data.

In the quartzite mylonite samples, the EBSD grain boundary maps closely match petrographic observations: the grain population can be subdivided into larger relic grains (> 250 μm) and recrystallized grains ranging in size from 20 to 75 μm (Figure 8A-D). Relic grains are typically mantled by recrystallized grains, and show many subgrains, confirming that subgrain rotation recrystallization is the dominant deformation mechanism in quartz. The quartz c-axis fabrics show a typical Type-I cross-girdle (Schmid and Casey, 1986). Samples RR09-11 (Figure 8A) and RR09-128 (Figure 8D) display broad slightly asymmetrical girdle, with components of basal, prism and rhomb <a> slip (Schmid and Casey, 1986). Samples RR09-15 (Figure 8B) and RR09-125 (Figure 8C) show a narrower gridle, with stronger component of rhomb <a> slip and more pronounced asymmetry.

In the vein samples, the analyzed areas are dominated by large quartz grains (Figure 8E, F). The large grains contain numerous subgrains, corroborating petrographic observations. Numerous small (< 20 μm), recrystallized grains are found at the periphery of the large grains. Interestingly, the c-axis polefigure indicates that the dominant active slip system in these quartz veins was prism <a> (Figure 8E, F).

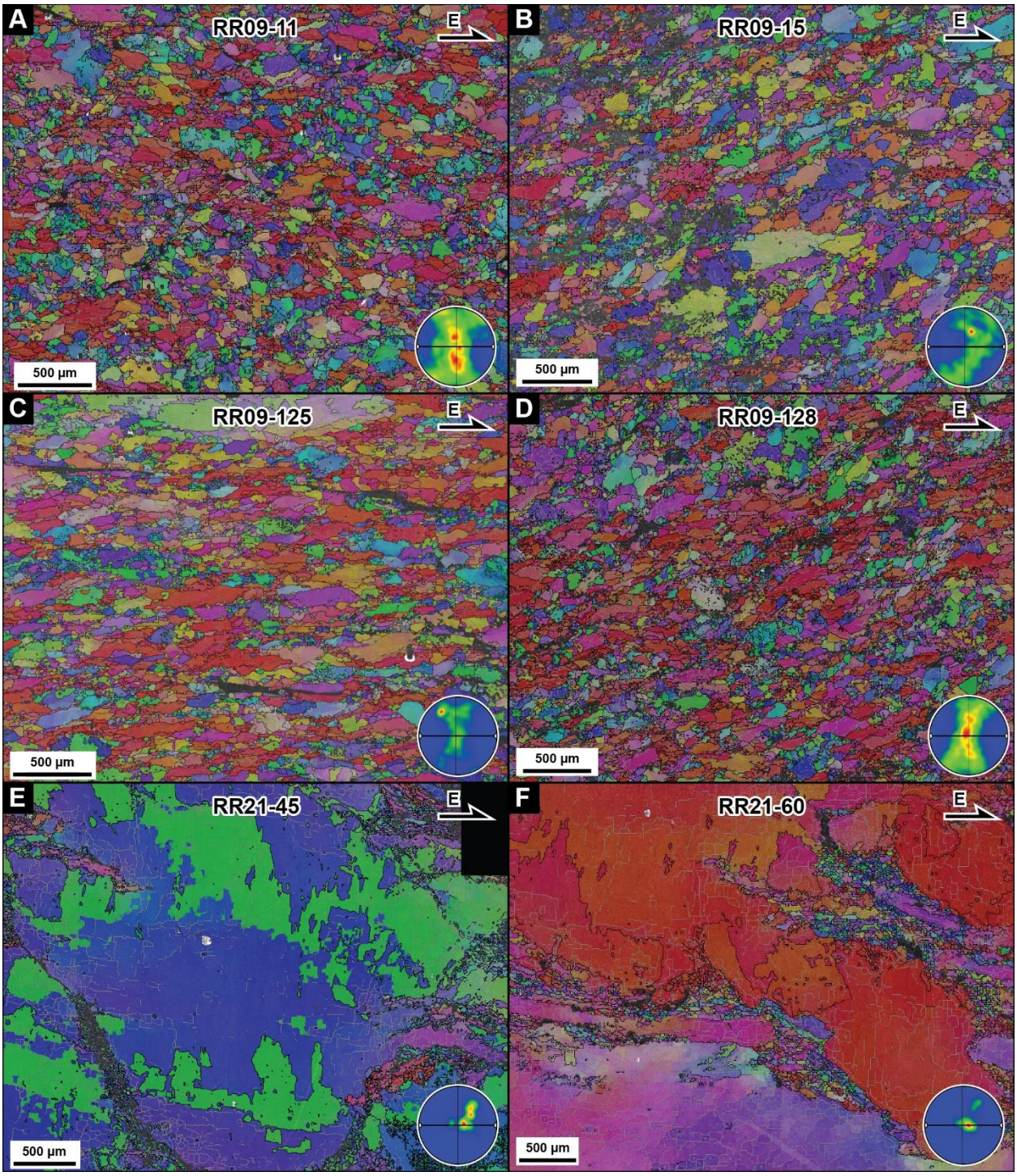

Figure 8: Detailed EBSD grain maps for mylonites (A-D), low angle veins (E), and high angle veins (F) showing grains in random colors. Black lines are grain boundaries, grey lines are subgrain boundaries. Each image contains a quartz c-axis polefigure for the samples. Samples oriented perpendicular to the foliation and parallel to the lineation, with a top-to-the-eat sense of shear.

5.4.FTIR Results

The FTIR data provides a complete absorbance spectra for each analyzed point on a sample. In this study, we are interested in the absorbance peak at ~3400 cm^{-1} associated with OH from molecular water and the ~1650 cm^{-1} peak characteristic of water (H_2O) trapped in fluid inclusions (e.g., Kronenberg et al., 2017). We present maps of these two absorbance peaks, along with cross-polarized petrographic images and cathodoluminescence images of the same area for reference (Figures 9-11).

In the high angle vein (RR21-60) – representing the least strained sample – the FTIR maps closely matches the observed microstructures (Figure 9). Molecular water (OH) content is lowest in the core of large, blocky grains (~700 ppm), and highest in areas of finely recrystallized/comminuted grains (~4300 ppm) (Table 2). Areas affected by subgrain rotation recrystallization show patchy OH distribution (Figure 9). Fractures show high OH and H_2O content, but we suspect that this may be caused by leftover epoxy that seeped into the crack and could not be properly removed during sample preparation. This is also true for some of the round blobs showing both high OH and H_2O content, that we associate with pits on the sample surface filled with leftover epoxy. The H_2O map shows a few blobs with high water content that are also visible in the OH map: we associate these features with the large fluid inclusion clusters that we observe on the petrographic images. The H_2O maps suggest that most grain boundaries contain a substantial amount of water in fluid inclusion form (Figure 9).

Similar trends can be observed in the low angle veins (RR21-01, -37, -45, -69), which represent our medium strained samples. The OH map highlights the dominant microstructures. The core of large blocky grains shows the lowest OH (~600-970 ppm) and H_2O content, while grain boundaries and areas associated with recrystallized grains show the highest OH content (up to ~5700 ppm) (Figure 10, Table 2). Grain boundaries can almost be traced on the OH map. Similarly to sample RR21-60 described previously for high angle veins, there are fractures and blobs of both very high OH and high H_2O that we associate with areas where epoxy was leftover.

Finally, mylonite samples (RR09-10, -11, -15, -125, -128, -132), the most strained samples, show low OH and H_2O content (Figure 11). The core of relic grains shows the lowest OH (as low as ~475 ppm). Grain boundaries are associated with slightly higher OH content (~1800-2800 ppm) (Table 2). We note again a few patches with high OH/ H_2O content, that we associate with leftover epoxy.

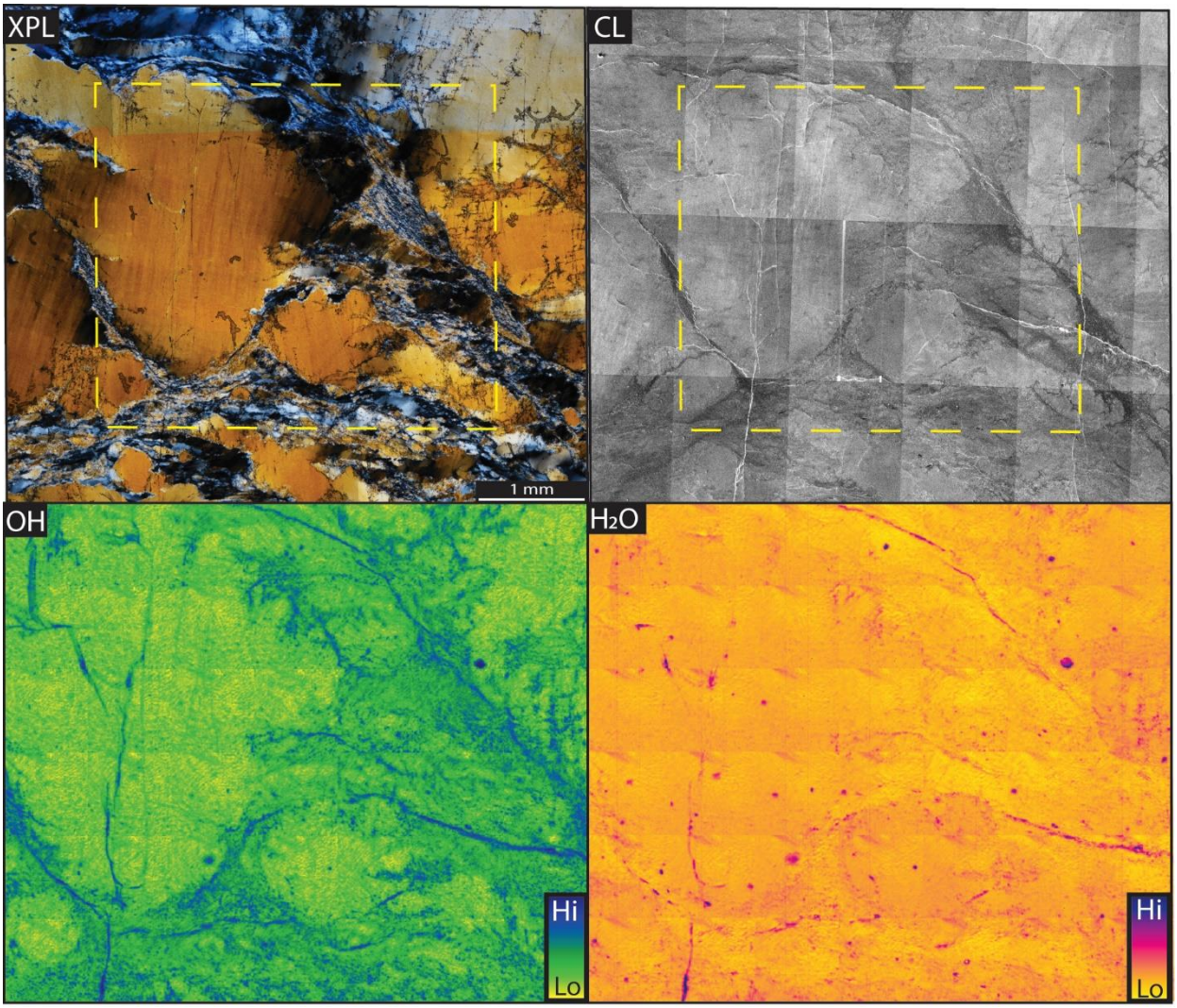

Figure 9: Compilation of cross polarized photomicrograph (XPL), cathodoluminescence (CL), and maps of the ~3400 cm^{-1} associated with OH from molecular water (OH), and ~1650 cm^{-1} is associated with water (H_2O) for sample RR21-60. The area investigated by FTIR is highlighted by the dashed yellow line in the XPL and CL images for reference. Sample RR21-60 is a high angle vein recording the least amount of strain.

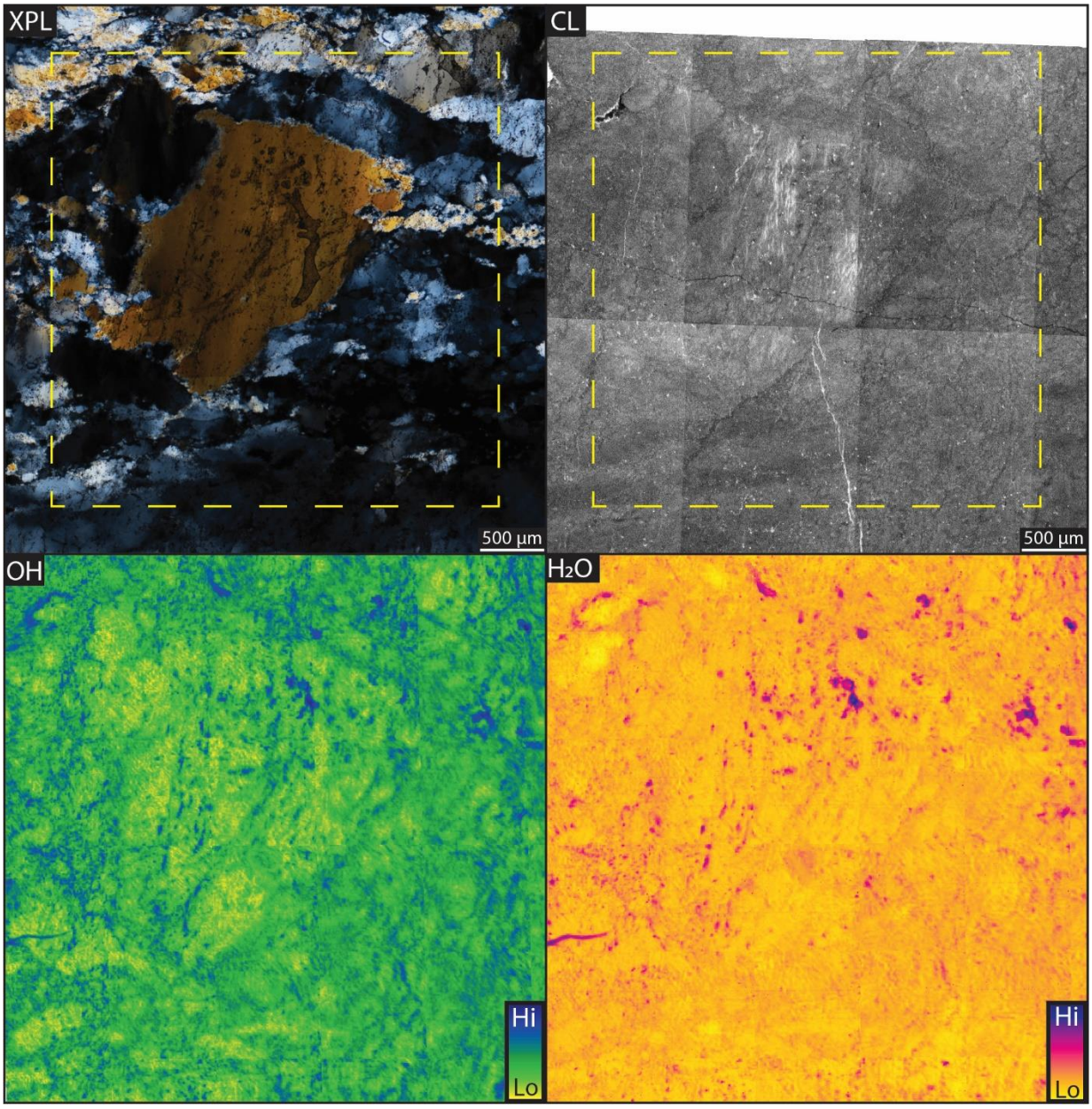

Figure 10: Compilation of cross polarized photomicrograph (XPL), cathodoluminescence (CL), and maps of the ~3400 cm^{-1} associated with OH from molecular water (OH), and ~1650 cm^{-1} is associated with water (H_2O) for sample RR21-69. The area investigated by FTIR is highlighted by the dashed yellow line in the XPL and CL images for reference. Sample RR21-69 represents a low angle vein, associated with moderate amount of strain.

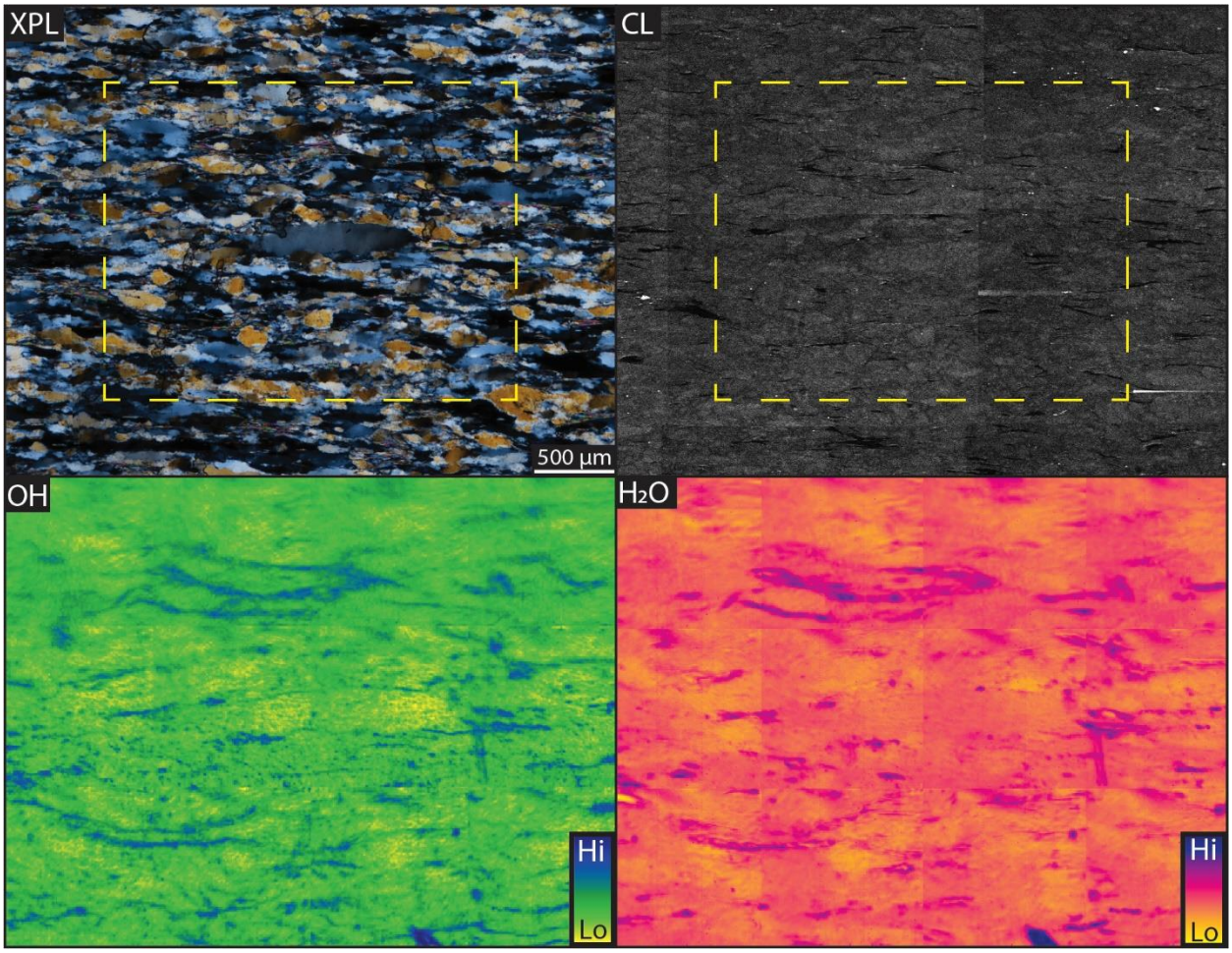

Figure 11: Compilation of cross polarized photomicrograph (XPL), cathodoluminescence (CL), and maps of the ~3400 cm^{-1} associated with OH from molecular water (OH), and ~1650 cm^{-1} is associated with water (H_2O) for sample RR09-132. The area investigated by FTIR is highlighted by the dashed yellow line in the XPL and CL images for reference. Sample RR09-10 is a mylonite, representing the most deformed of our samples.

Table 2: Estimated water concentration using the Beer-Lambert equation (Stuart et al., 1996), using the height of the 3400 cm^{-1} peak at different areas in our samples specifically grain interiors, grain boundaries, and areas of recrystallized grains. We used an approximate sample thickness of 80 μm.

Sample	Rock type	OH concentration (molar ppm)		
		Grain interior	Grain boundary	Recrystallized grain
RR09-10	Mylonite	475	1896	2629
RR09-11	Mylonite	1620	2857	2442
RR09-15	Mylonite	1606	1826	2567
RR09-125	Mylonite	1610	1884	2647
RR09-128	Mylonite	-	1065	7489
RR09-132	Mylonite	1524	2268	1471
RR21-01	Low angle Vein	902	2318	3884
RR21-37	Low angle Vein	881	1993	5405
RR21-45	Low angle Vein	591	2028	3841
RR21-69	Low angle vein	968	3167	5732
RR21-60	High-angle vein	699	1676	4320

6. DISCUSSION

To investigate the effects of water on quartz deformation processes in the Miocene RRDSZ, we used the degree of dynamic recrystallization of each sample as a proxy for strain (e.g., Cross and Skemer, 2019), and selected high angle quartz veins, low angle quartz veins, and quartzite mylonite, representing low, moderate, and high strain samples, respectively characterized by < 10%, < 40%, and up to 50% of dynamically recrystallized quartz grains). All of these samples have available quartz oxygen stable isotope composition that we used to infer degrees of fluid-rock interaction (Table 1). We used a comprehensive sequence of analyses including petrography, SEM-CL, EBSD, and FTIR spectroscopy to first investigate the relationship between deformation microstructures and water related processes in our samples. We then use our results to further constrain water circulation in mid-crustal ductile shear zones.

6.1. Cathodoluminescence intensity as a microstructural indicator for quartz

SEM-CL has been used to reveal a wide range of textures that can be used to relate quartz microstructures to vein-host rock interactions, fluid inclusion populations, isotopic compositions, or trace-element content (e.g., Rusk et al., 2006 and references therein). Across all our samples, SEM-CL is closely associated with quartz microstructures and progressive dynamic recrystallization. Generally, in both types of vein samples (high and low angle), the core of large, blocky grains and quartz ribbons tend to show high CL intensity, while areas of recrystallized grains tend to be darker (Figures 6-7). In both high angle and low angle veins, the recrystallized grains are notably less luminescent than the relic grains and appear dark in CL images (Figures 6-7). This observation is also true in the quartzite mylonite, where relic grains tend to have cores associated with bright CL and darker rims, while recrystallized grains appear much darker in CL (Figure 7). Lattice defects, such as undulatory extinction and deformation bands are also visible in CL (Figure 6-7). In general, we observe that increasing deformation and recrystallization generates less luminescence, i.e., the mylonites are overall less luminescent than the veins.

The origin of this decreasing trend of CL intensity with increasing macroscopic deformation may be related to two processes: (1) dislocation density and/or the density of point defects or (2) grain boundary migration by dissolution precipitation (e.g., Shimamoto et al., 1990). CL emission has been associated at least partly with mineral defect content: high dislocation density is associated with high CL while low dislocation density produces low CL (Marshall, 1988). Hence, the

observed trend of decreasing CL intensity with increasing dynamic recrystallization is consistent with low CL emission from the areas of recrystallized grains, as recrystallization and recovery processes lower dislocation density (e.g., Passchier and Trouw, 2005). On the other hand, the core of relic grains in the mylonite and the large blocky grains in the veins display strong internal lattice deformation, likely associated with high dislocation/defect density, indicated by the presence of undulose extinction, numerous subgrains, and deformation lamellae (Figures 6-7). Additionally, grain boundary migration is a process assisted by dissolution-precipitation (e.g., Greene et al., 2009; Thomas and Nachlas, 2020). Dissolution-precipitation produces nearly defect-free grains or defect free grain boundaries around relic grains (e.g., Ghosh et al., 2024; Stünitz et al., 2017, 2024). As such, we would expect these areas to emit low CL. Dissolution-precipitation has previously been described in the RRDSZ (and others) as a necessary mechanism to produce synkinematic muscovite in the mylonite (Gottardi and Teyssier, 2013, Gottardi et al., 2015). Oxygen and hydrogen stable isotope geochemical analyses demonstrate significant fluid-rock-deformation interaction during ductile deformation of the RRDSZ suggesting that fluids were abundant during the development of the shear zone (Gottardi et al., 2011; 2015; 2024; Methner et al., 2015). Therefore, we suggest that the darker CL in our samples is the result of the low defect density in quartz, produced by a combination of dynamic recrystallization by subgrain rotation and dissolution-precipitation at the grain boundaries in a fluid saturated system.

6.2.Water infiltration in the shear zone

Previous oxygen and hydrogen stable isotope studies of quartz-muscovite pairs have demonstrated that surface-derived meteoric fluid percolated through the brittle upper and interacted with deforming rocks in the footwall of the Raft River detachment shear zone (Gottardi et al., 2011, 2015, 2024; Methner et al., 2015). While cataclasis and faulting can greatly enhance fluid circulation in the brittle regime by increasing porosity and permeability, how surface-derived fluids gets pumped beyond the brittle-ductile transition is, however, a complex physio-mechanical process (e.g. Connolly and Podladchikov, 2004; Fusseis et al., 2009; Lyubetskaya and Ague, 2009; Yardley, 2009; Menegon et al., 2015; Gilgannon et al., 2020; Schmalholz et al., 2024). In the following, we discuss how our combined microstructural, CL, and FTIR results shed some light on fluid (re)distribution in the ductile regime, and how fluids may be able to circulate in the deep crust.

High angle veins are composed of large (mm-size) blocky quartz grains separated by either recrystallized grains or thin deformation bands associated with grain comminution, that we interpret to reflect cataclastic bands (Figure 3). Blocky quartz is riddled with plastic defects, including undulose extinction, deformation lamellae and numerous subgrains. Incipient dynamic recrystallization is evident around large grains. The core of the large grains, characterized by bright CL, shows some of the lowest OH content (~700 ppm) measured across all our samples (Table 2). Yet, in these same samples, areas of very fine grains associated with dark CL show some of the highest OH content (>4300 ppm) (Table 2). These high angle vein samples also contain numerous healed fractures riddled with fluid inclusions, as well as fluid inclusion clusters distributed along the grain boundaries of larger grains.

In the low angle veins, progressive recrystallization by dislocation creep is evident: large blocky grains are progressively recrystallized by subgrain rotation (Figures 4 and 8). FTIR maps show a more complex pattern, with patches of low OH/high CL surrounded by subgrain boundaries associated with OH enrichment (dark CL): relic grains develop a grain boundary area that is enriched on OH (~>2000 ppm) compared to the core (~900 ppm) (Table 2; Figures 6 and 10). Recrystallized grains have the highest OH content measured in these samples as well (up to ~5700 ppm) (Table 2). As mentioned in Section 6.1., the development of a darker CL rim around relic grains could result from a combination of reduction of defect density through recrystallization and dissolution precipitation processes. With OH available around the larger grains, either of these processes could eventually lead to enrichment of the quartz grains in OH at grain and subgrain boundaries, through progressive recrystallization or dissolution-precipitation, leading to the patchy OH pattern observed among relic grains in these samples (Figure 10C).

The quartzite mylonite represents the most deformed of our samples. We observe similar CL and OH distribution across all mylonitic samples: relic grains tend to have bright CL/low OH content, while recrystallized grains tend to have dark CL/high OH content. Relic grains show a grain boundary area that is darker than the core in CL and contains higher OH (up to ~2800 ppm) than the core (~1600 ppm) (Table 2). The recrystallized grains have the highest OH content in these samples as well (~1400 to ~2600 ppm). Interestingly, the core of relics in the mylonite contains almost twice the amount of OH (~1600 ppm) compared to the vein samples (~600-~900 ppm) (Table 2). Additionally, both the CL and the OH distribution across relic grains core and rim are very similar in both the mylonite and the low angle veins, suggesting similar OH

redistribution processes. Therefore, we suggest that in the mylonite as well, OH present in the recrystallized grains or at the grain boundaries is progressively dispersed through a combination of dynamic recrystallization and dissolution-precipitation. Because the mylonite samples are extensively recrystallized, both the CL and OH pattern become more diffuse, as recrystallization and dissolution-precipitation lead to progressive homogenization of OH through the mineral aggregate (Figure 11C).

6.3.Implication for water infiltration in shear zones

Previous structural, microstructural, and geochemical studies have documented the dynamic interplay between crystal-plastic and brittle deformation during Miocene exhumation of the RRDSZ, providing important insights into fluid circulation beyond the brittle regime at mid-crustal depths (Gottardi et al., 2011, 2015, 2024; Gottardi and Teyssier; Methner et al., 2015; Gottardi and Hughes. 2022). Microstructural analysis shows that quartz primarily deformed by dislocation creep and subgrain rotation at temperatures of ~450–500°C, near the brittle-ductile transition (Figure 3-5, see also Gottardi et al., 2011; Gottardi and Teyssier, 2013). Quartz microstructures commonly display undulose extinction and deformation lamellae, indicative of high stress/ high strain rate deformation conditions (Figures 3-5; see also Gottardi and Teyssier, 2013). These ductile fabrics are overprinted by brittle structures, including various generations of quartz veins that are plastically deformed. The quartzite mylonite also preserves healed microfractures and various fluid inclusion populations (see Section 5.1.2.), reflecting episodic changes in the stress field (Gottardi and Hughes, 2022). These microstructures have been interpreted to reflect stress buildup leading to periodic brittle failure, which allowed surface-derived fluids to enter the shear zone, followed by post-seismic healing and continued ductile deformation that trapped and redistributed fluid inclusions (Gottardi and Hughes, 2022). This cycle likely repeated multiple times during exhumation, promoting fluid flow and fluid redistribution through fluid inclusions in the evolving shear zone. This mechanism, referred to as “seismic pumping”, may be one of the primary drivers of the seismic cycle (Sibson, 1977; McCaig, 1988; Cox, 2010; Zhu et al., 2020; Prando et al., 2020, Menegon and Fagereng, 2021).

This model was developed on the basis of structural, microstructural, and geochemical observations, yet it was missing a consideration of where and how fluids are distributed across

the shear zone. The combined CL and FTIR results discussed in Section 6.2. help further constrain the mechanisms of fluid distribution in the plastically deforming shear zone.

As previous studies suggest, high stress microstructures (undulose extinction, deformation lamellae, deformation bands) suggest that the RRDSZ evolved at its peak strength, and indicate that the rate of recovery in the quartzite mylonite was not sufficiently rapid to keep up with strain rate and offset strain hardening, embrittlement, and eventually seismic failure (Gottardi and Teyssier, 2013; Gottardi and Hughes, 2022). Brittle failure would lead to the formation of quartz vein and provide opportunity for fluids to enter the shear zone, leading to highly localized fluid entrapment along fractures. This is documented by the high OH content (3,800 to 5,700 ppm) and low CL associated with the comminuted grains in the high angle quartz veins (Figure 9). Post-seismic relaxation causes healing of the quartz veins while renewed stress accumulation and high temperature (~450–500°C) promote dislocation creep. As deformation accumulates, fluids trapped in the cataclastic bands are redistributed through a combination of subgrain rotation recrystallization and dissolution-precipitation creep, as evidenced by the development of high CL/low OH cores and low CL/low OH rims (Figure 10). As recrystallization proceeds, fluids become further redistributed by these two processes, and water content in the mylonite is progressively homogenized, leading to lesser OH content variation, and subtle CL gradients across relic grains and recrystallized subgrains (Figure 11). We envision that this cycle of episodic fluid intake and fluid dissemination may have been repeated several times during the exhumation of the RRDSZ.

7. CONCLUSIONS

This study provides new insights into the role of fluids in controlling quartz deformation within the Raft River detachment shear zone by integrating microstructural, crystallographic, and spectroscopic analyses. Our results demonstrate that quartz deformation across all lithologies is dominated by dislocation creep accommodated by subgrain rotation recrystallization, independent of bulk water content. FTIR data reveal that water is preferentially concentrated along grain boundaries and within recrystallized domains, whereas grain interiors remain comparatively dry. Our results show that progressive deformation, accommodated by dislocation creep and dissolution-precipitation, leads to redistribution and homogenization of the water content. These observations challenge simple models of hydrolytic weakening based solely on

bulk water concentration and instead emphasize the critical role of water distribution at the microscale. This work highlights the dynamic interplay between deformation at the brittle-ductile transition, recrystallization, and fluid circulation, and underscores the importance of microstructural controls in governing the mechanical behavior of the mid-crust.

REFERENCES

Berthomieu, C., & Hienerwadel, R. (2009). Fourier transform infrared (FTIR) spectroscopy. Photosynthesis research, 101(2), 157-170.

Bürgmann, R., & Dresen, G. (2008). Rheology of the lower crust and upper mantle: Evidence from rock mechanics, geodesy, and field observations. Annu. Rev. Earth Planet. Sci., 36(1), 531-567.

Ceccato, A., Menegon, L., & Hansen, L. N. (2022). Strength of dry and wet quartz in the low-temperature plasticity regime: Insights from nanoindentation. Geophysical Research Letters, 49(2), e2021GL094633.

Chacko, T., Hu, X., Mayeda, T. K., Clayton, R. N., & Goldsmith, J. R. (1996). Oxygen isotope fractionations in muscovite, phlogopite, and rutile. Geochimica et Cosmochimica Acta, 60(14), 2595-2608.

Cox, S. F. (2010). The application of failure mode diagrams for exploring the roles of fluid pressure and stress states in controlling styles of fracture-controlled permeability enhancement in faults and shear zones. Geofluids, 10(1-2), 217-233.

Cross, A. J., and P. Skemer (2019). Rates of dynamic recrystallization in geologic materials. Journal of Geophysical Research: Solid Earth 124.2: 1324-1342.

Demsar J, Curk T, Erjavec A, Gorup C, Hocevar T, Milutinovic M, Mozina M, Polajnar M, Toplak M, Staric A, Stajdohar M, Umek L, Zagar L, Zbontar J, Zitnik M, Zupan B (2013) Orange: Data Mining Toolbox in Python Journal of Machine Learning Research 14(Aug):2349−2353.

Derez, T., Pennock, G., Drury, M., & Sintubin, M. (2015). Low-temperature intracrystalline deformation microstructures in quartz. Journal of Structural Geology, 71, 3-23.

Frelinger, S. N., Ledvina, M. D., Kyle, J. R., & Zhao, D. (2015). Scanning electron microscopy cathodoluminescence of quartz: Principles, techniques and applications in ore geology. Ore Geology Reviews, 65, 840-852.

Fukuda, J. I., & Shimizu, I. (2019). Water distribution in quartz schists of the Sanbagawa Metamorphic Belt, Japan: infrared spectroscopic mapping and comparison of the calibrations proposed for determining water contents. Earth, Planets and Space, 71(1), 136.

Gleason, G. C., & DeSisto, S. (2008). A natural example of crystal-plastic deformation enhancing the incorporation of water into quartz. Tectonophysics, 446(1-4), 16-30.

Ghosh, S., Stünitz, H., Raimbourg, H., Précigout, J., Di Carlo, I., Heilbronner, R., & Piani, L. (2024). Importance of grain boundary processes for plasticity in the quartz-dominated crust: Implications for flow laws. Earth and Planetary Science Letters, 640, 118767.

Gottardi, R., & Hughes, B. (2022). Role of fluids on deformation in mid-crustal shear zones, Raft River Mountains, Utah. Geological Magazine, 159(11-12), 2206-2218.

Gottardi, R., & Teyssier, C. (2013). Thermomechanics of an extensional shear zone, Raft River metamorphic core complex, NW Utah. Journal of Structural Geology, 53, 54-69.

Gottardi, R., Teyssier, C., Mulch, A., Vennemann, T. W., & Wells, M. L. (2011). Preservation of an extreme transient geotherm in the Raft River detachment shear zone. Geology, 39(8), 759-762.

Gottardi, R., Teyssier, C., Mulch, A., Valley, J. W., Spicuzza, M. J., Vennemann, T. W., ... & Heizler, M. (2015). Strain and permeability gradients traced by stable isotope exchange in the Raft River detachment shear zone, Utah. Journal of Structural Geology, 71, 41-57.

Gottardi, R., Mire, C., Davis, N., & Casale, G. (2024). Effect of water-rock ratio on the stable isotope record of fluid-rock-deformation interactions in detachment shear zone. Geochemistry, Geophysics, Geosystems, 25(5), e2023GC011340.

Greene, G. W., Kristiansen, K., Meyer, E. E., Boles, J. R., & Israelachvili, J. N. (2009). Role of electrochemical reactions in pressure solution. Geochimica et Cosmochimica Acta, 73(10), 2862-2874.

Griggs, D. (1967). Hydrolytic weakening of quartz and other silicates. Geophysical Journal International, 14(1-4), 19-31.

Griggs, D. T., & Blacic, J. D. (1965). Quartz: Anomalous weakness of synthetic crystals. Science, 147(3655), 292-295.

Kilian, R., Heilbronner, R., Holyoke III, C. W., Kronenberg, A. K., & Stünitz, H. (2016). Dislocation creep of dry quartz. Journal of Geophysical Research: Solid Earth, 121(5), 3278-3299.

Kronenberg, A. K., & Wolf, G. H. (1990). Fourier transform infrared spectroscopy determinations of intragranular water content in quartz-bearing rocks: implications for hydrolytic weakening in the laboratory and within the earth. Tectonophysics, 172(3-4), 255-271.

Kronenberg, A. K., Ashley, K. T., Francsis, M. K., Holyoke III, C. W., Jezek, L., Kronenberg, J. A., ... & Thomas, J. B. (2020). Water loss during dynamic recrystallization of Moine thrust quartzites, northwest Scotland. Geology, 48(6), 557-561.

Kronenberg, A. K., Hasnan, H. F., Holyoke III, C. W., Law, R. D., Liu, Z., & Thomas, J. B. (2017). Synchrotron FTIR imaging of OH in quartz mylonites. Solid Earth, 8(5), 1025-1045.

Hatherington, G. (1962). Water in vitreous silica Part 1. Influence of water content on the properties of vitreous silica. Physics and Chemistry of Glasses, 3, 129-133.

Hirth, G., & Tullis, J. A. N. (1992). Dislocation creep regimes in quartz aggregates. Journal of structural geology, 14(2), 145-159.

Hirth, G., Teyssier, C., & Dunlap, J. W. (2001). An evaluation of quartzite flow laws based on comparisons between experimentally and naturally deformed rocks. International Journal of Earth Sciences, 90(1), 77-87.

Lallemant, H. A., & Carter, N. L. (1971). Pressure dependence of quartz deformation lamellae orientations. American Journal of Science, 270(3).

McCaig, A. M. 1988. Deep fluid circulation in fault zones. Geology 16, 867–870.

Menegon, L., & Fagereng, Å. (2021). Tectonic pressure gradients during viscous creep drive fluid flow and brittle failure at the base of the seismogenic zone. Geology, 49(10), 1255-1259.

Methner, K., Mulch, A., Teyssier, C., Wells, M.L., Cosca, M.A., Gottardi, R., Gébelin, A. and Chamberlain, C.P. (2015). Eocene and Miocene extension, meteoric fluid infiltration, and core complex formation in the Great Basin (Raft River Mountains, Utah). Tectonics, 34(4), pp.680-693.

Nakashima, S., Matayoshi, H., Yuko, T., Michibayashi, K., Masuda, T., Kuroki, N., Yamagishi, H., Ito, Y. and Nakamura, A., 1995. Infrared microspectroscopy analysis of water distribution in deformed and metamorphosed rocks. Tectonophysics, 245(3-4), pp.263-276.

Nichols, A. R., & Wysoczanski, R. J. (2007). Using micro-FTIR spectroscopy to measure volatile contents in small and unexposed inclusions hosted in olivine crystals. Chemical Geology, 242(3-4), 371-384.

Palazzin, G., Raimbourg, H., Stünitz, H., Heilbronner, R., Neufeld, K., & Précigout, J. (2018). Evolution in H2O contents during deformation of polycrystalline quartz: An experimental study. Journal of Structural Geology, 114, 95-110.

Paterson, M. (1982). The determination of hydroxyl by infrared absorption in quartz, silicate glasses and similar materials. Bulletin de minéralogie, 105(1), 20-29.

Pongrac, P., Jeřábek, P., Stünitz, H., Raimbourg, H., Racek, M., Jollands, M.C., Gies, N., Lueder, M., Lexa, O. and Nègre, L. (2024). Mechanical impact of heterogeneously distributed H2O on quartz deformation. Journal of Geophysical Research: Solid Earth, 129(8), p.e2023JB027566.

Prando, F., Menegon, L., Anderson, M., Marchesini, B., Mattila, J., & Viola, G. (2020). Fluid-mediated, brittle–ductile deformation at seismogenic depth–Part 2: Stress history and fluid pressure variations in a shear zone in a nuclear waste repository (Olkiluoto Island, Finland). Solid Earth, 11(2), 489-511.

Rahl, J. M., Moehringer, B., Befus, K. S., & Singleton, J. S. (2024). Influence of water on crystallographic preferred orientation patterns in a naturally deformed quartzite. Solid Earth, 15(10), 1233-1240.

Rusk, B. G., Reed, M. H., Dilles, J. H., & Kent, A. J. (2006). Intensity of quartz cathodoluminescence and trace-element content in quartz from the porphyry copper deposit at Butte, Montana. American Mineralogist, 91(8-9), 1300-1312.

Schmalholz, S. M., Khakimova, L., Podladchikov, Y., Bras, E., Yamato, P., & John, T. (2024). (De) hydration front propagation into zero-permeability rock. Geochemistry, Geophysics, Geosystems, 25(9), e2023GC011422.

Schmid, S. M., & Casey, M. (1986). Complete fabric analysis of some commonly observed quartz c-axis patterns. Mineral and rock deformation: Laboratory studies, 36, 263-286.

Sibson, R. H. (1977). Fault rocks and fault mechanisms. Journal of the Geological Society, 133(3), 191-213.

Stuart, B. H., George, B., and McIntyre, P.: Modern Infrared Spectroscopy, J. Wiley and Sons, 200 pp., 1996.

Stünitz, H., Thust, A., Heilbronner, R., Behrens, H., Kilian, R., Tarantola, A., & Fitz Gerald, J. D. (2017). Water redistribution in experimentally deformed natural milky quartz single crystals—Implications for H2O-weakening processes. Journal of Geophysical Research: Solid Earth, 122(2), 866-894.

Stünitz, H., Raimbourg, H., Nègre, L., Précigout, J., Jollands, M., Pongrac, P., ... & Lüder, M. (2024). Evolution of H2O content in deforming quartz aggregates: An experimental study. Journal of Structural Geology, 178, 105029.

Sullivan, W. A. (2008). Significance of transport-parallel strain variations in part of the Raft River shear zone, Raft River Mountains, Utah, USA. Journal of Structural Geology, 30(2), 138-158.

Thomas, J. B., & Nachlas, W. O. (2020). Discontinuous precipitation of rutilated quartz: grain-boundary migration induced by changes to the equilibrium solubility of Ti in quartz. Contributions to Mineralogy and Petrology, 175(4), 38.

Tullis, J., & Yund, R. A. (1980). Hydrolytic weakening of experimentally deformed Westerly granite and Hale albite rock. Journal of Structural Geology, 2(4), 439-451.

Wells, M. L. (1997). Alternating contraction and extension in the hinterlands of orogenic belts: An example from the Raft River Mountains, Utah. Geological Society of America Bulletin, 109(1), 107-126.

Wells, M. L., Snee, L. W., & Blythe, A. E. (2000). Dating of major normal fault systems using thermochronology: An example from the Raft River detachment, Basin and Range, western United States. Journal of Geophysical Research: Solid Earth, 105(B7), 16303-16327.

Zhu, W., Allison, K. L., Dunham, E. M., & Yang, Y. (2020). Fault valving and pore pressure evolution in simulations of earthquake sequences and aseismic slip. Nature communications, 11(1), 1-11.